High-z Sudoku: A diagnostic tool for identifying robust sub-mm redshifts

Tom J. L. C. Bakx[1,2][*] and Helmut Dannerbauer[3,4]

[1] *Division of Particle and Astrophysical Science, Graduate School of Science, Nagoya University, Aichi 464-8602, Japan.*

[2] *National Astronomical Observatory of Japan, 2-21-1, Osawa, Mitaka, Tokyo 181-8588, Japan.*

[3] *Instituto Astrofísica de Canarias (IAC), E-38205 La Laguna, Tenerife, Spain.*

[4] *Universidad de la Laguna, Dpto. Astrofísica, E-38206 La Laguna, Tenerife, Spain.*

ABSTRACT

We present a graphical method to help identify robust redshifts using emission lines in the submm regime. Using this publicly-available code, we discuss scenarios where robust redshifts can be identified using both single- and multiple-line detections, as well as scenarios where the redshift remains ambiguous, even after the detection of multiple lines. Using the known redshift distribution of submm samples, we use this to quantify the efficiencies of various typically-used redshift instruments an using heterodyne interferometers (i.e., Atacama Large Millimetre/submillimetre Array) and so-called redshift hunters on single-dish instruments. Finally, we provide a method to optimise ones observation windows for a redshift search based on the sources' expected redshift distribution.

Key words: keyword1 – keyword2 – keyword3

1 INTRODUCTION

Since their discovery in the 1990's, sub-millimetre galaxies (SMGs) have been difficult to square with our picture of galaxy evolution (see e.g., Blain et al. 2002; Casey et al. 2014). Their strong emission in submm wavelengths implied star-formation rates in excess of $1000\,\mathrm{M_\odot}$/yr, approaching or exceeding the limits of stable galaxy systems through excessive feedback (Rowan-Robinson et al. 2016), while their strong dust-obscuration posed serious challenges to large-scale unbiased follow-up attempts across all wavelengths (Casey et al. 2018).

A first step towards such follow-up requires precise and robust redshift measurements. Unfortunately, photometric redshifts from submm colours remain only indicative of a redshift range (Casey et al. 2012; Pearson et al. 2013; Ivison et al. 2016; Bakx et al. 2018) due to the degeneracy between dust temperature and redshift. Redshifts derived from spectroscopic lines break this degeneracy. The first redshift searches used optical spectral lines, however they struggled with the positional uncertainty of SMGs. Here, radio observations improved the positions, but provide a strong bias towards lower redshifts, and are not workable for large, complete redshift samples (e.g., Chapman et al. 2015). Instead, redshift searches using sub-millimetre spectroscopy are unhindered by dust extinction and can be related unambiguously to the (sub)millimetre source, offering a far better alternative to optical spectroscopy and to the imprecise submm photometric method. The submm spectroscopic method has only become competitive with the increased bandwidths of the receivers operating at mm and sub-mm facilities, as for example demonstrated by Weiß et al. (2013), who presented the first redshift survey for 23 strongly lensed dusty star-forming galaxies se-

lected from the South Pole Telescope (SPT) 2500 deg^2 survey using the Atacama Large Millimetre/submillimetre Array (ALMA).

The process of robust redshift determination at submm wavelengths, in particular using rotational emission lines from carbon-monoxide (CO), involves the careful comparison between the potential redshift solutions of individual lines and selecting the solution where multiple lines agree. This method is far from ideal, as it leads to confirmation bias for solutions close to the z_{phot} (Yanai & Lercher 2020), and fails to draw attention to redshift degeneracies. Instead, sometimes redshift solutions can be excluded if we fail to detect in additional spectral lines within the bandwidth. In this paper, we expand on the graphical method from Bakx et al. (2020b) which provides a more user-friendly method for identifying robust redshifts. This method is capable of highlighting redshift degeneracies, and enables the easy removal of untenable redshift solutions. We liken this approach to graphical-numerical puzzles, such as the Sudoku[1] puzzle mentioned in the title. We describe the method in detail in Section 2, where we explain different scenarios and note important caveats. In Section 3, we show how this method can be used to find the optimum tunings for future redshift searches. The code and example scripts for each of the graphs in this paper are publicly available at https://github.com/tjlcbakx/redshift-search-graphs, and can be easily adapted for the reader's own needs.

2 GRAPHICAL METHOD

Robust redshifts require the exclusion of any other potential redshift interpretations of the line emission except one. Numerically solving

---

[*] E-mail: bakx@a.phys.nagoya-u.ac.jp (Nagoya University)

[1] While invented in the USA, the late Maki Kaji (鍜治真起) popularized the game as **Sū**ji wa **doku**shin ni kagiru (数字は独身に限る), translating to *the digits must be single*.
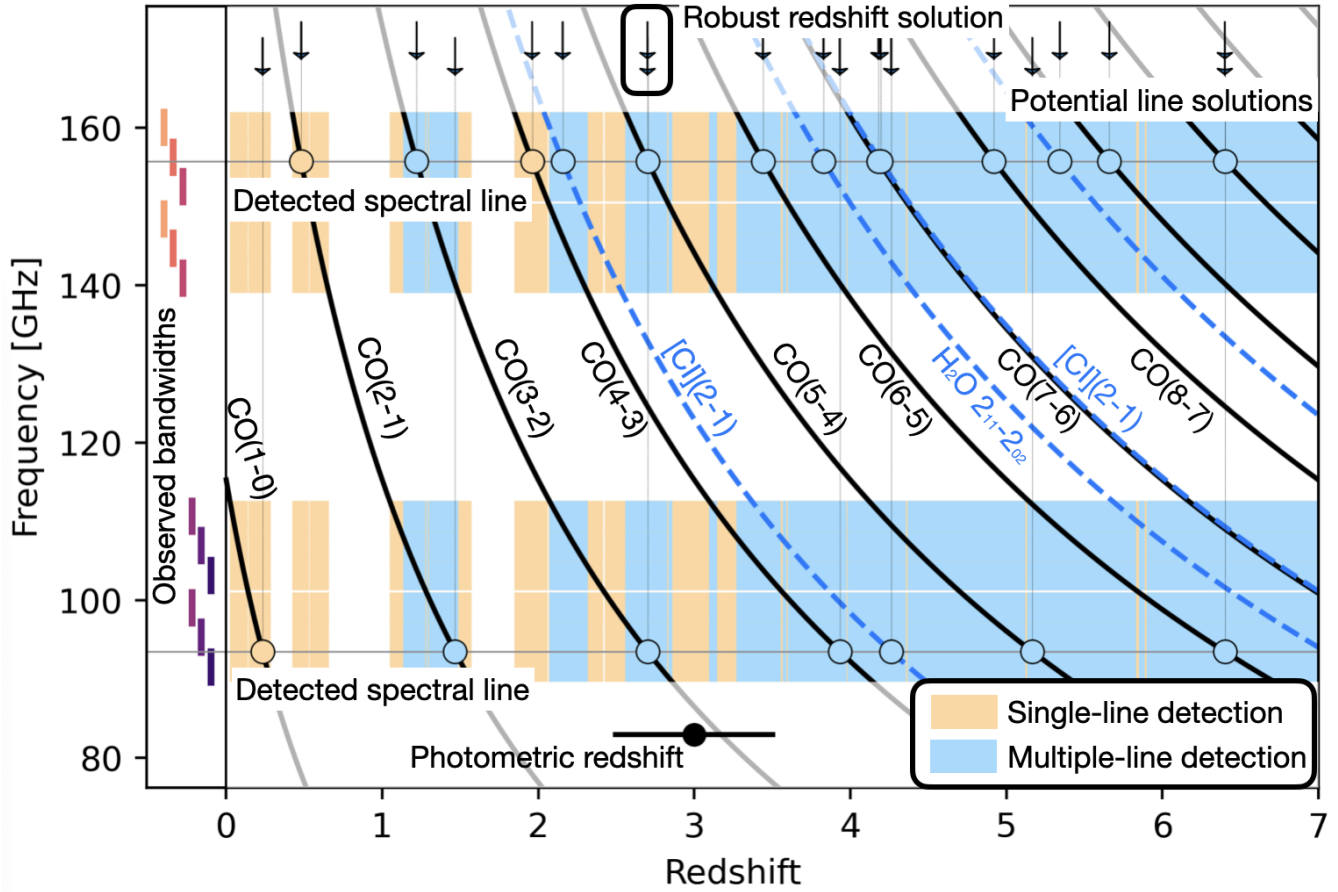
Figure 1. The graphical method reveals the full redshift space probed by submm observations. Assuming the observed bandwidths (*shown the left-hand side*), the filled regions show redshifts where single and multiple lines would be detected (*orange* and *blue*, resp.). The horizontal lines mark the observed lines, indicating the potential redshift solutions where they cross the observable lines (*circles*) with the fill matching the underlying colour. The *top arrows* indicate the position of these cross-over points, and a true multi-line redshift requires these arrows to line up. In this example, the two observed CO line transitions CO(3-2) and CO(5-4) result in a robust redshift identification at $z = 2.7$, since we can exclude all but one other solution where the two arrows do not line up. This other solution at $z \approx 6.4$ can be excluded through the lack of emission at 109.040 and 140.195 GHz.

this cross-comparison is a tedious approach, prone to errors and overlooked options. Instead, we use the following graphical method for identifying the potential spectroscopic redshifts for each line. We further detail several redshift identification examples, and list several caveats with this method specifically and redshift searches in general.

2.1 Explanation of the graphical method

In Figure 1, we show this graphical method for a fiducial $z_{phot} = 3$ example source observed with an efficient ALMA tuning setup (see Section 3). We show the observed frequency against the covered redshift. We expect to detect CO-lines, and potentially [C I] and H_2O lines, which we graph as *black* and *dashed blue* lines, respectively. Each actually-observed spectral line is indicated with a *horizontal line* at the observed frequency, and where they cross the redshifted spectral lines, we mark the potential spectroscopic redshift with a *circle* filled with its underlying colour and identify this potential spectroscopic redshift with an arrow in the top of the graph. On the left-hand side, we indicate the observed frequency bands within which we expect to detect all CO-lines. For this range of frequency coverage, we indicate whether the observations would be able to observe one or more spectral lines, indicated with *orange* and *blue*

fill, respectively. We do this only for the CO lines, as we typically cannot be certain the observations are deep enough to have detected the [C I] and H_2O emission (see Section 2.3.2). The *black point* below indicates the photometric redshift estimate, with its typical uncertainty in $\Delta z/(1 + z)$ of $\sim 13\%$ (Bakx et al. 2018; Casey 2020).

The top arrows line up when multiple lines agree on a robust redshift, identifying the spectroscopic redshift. This check is important, because CO-line redshift surveys can suffer from potential multiple redshift solutions (see below), since the CO-ladder increases linearly with each transition J_{up}. For example, the observation of $J_{up} = 2$ and 4 CO-line transitions of a $z = 2$ galaxy (76.7 and 153 GHz, resp.) could also be interpreted as the $J_{up} = 3$ and 6 CO-line transitions of a $z \approx 3.5$ galaxy. This mis-identification is a non-negligible possiblity given the large 13% errors in sub-mm derived photometric redshifts of around $\Delta z \sim 1$ (e.g. Pearson et al. 2013; Ivison et al. 2016; Bakx et al. 2018).
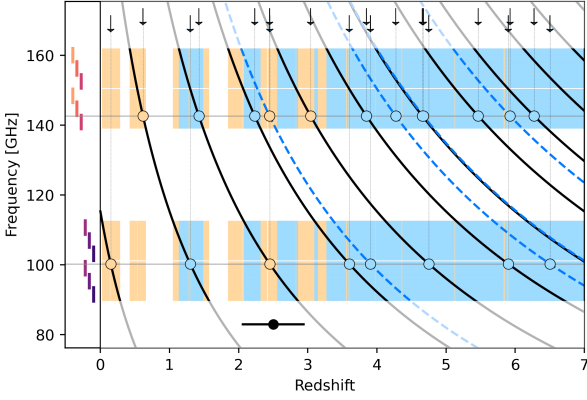
Figure 2. Same as Fig. 1, showing a robust redshift identification using a combination of CO and [C I] emission. Because non-CO lines do not follow the linear scaling of CO emission lines, any combination of a redshift identification using CO and such additional lines removes the possibility of inconclusive redshifts due to degeneracy in the CO transitions.

Figure 3. Same as Fig. 1, showing a robust redshift at $z = 3.0$ using just a single spectral line. Here, we require that the single spectral line is observed at high significance ($>8\sigma$), with no detectable emission at any of the potential line solutions. The low-redshift solution can often times be excluded through optical or near-infrared follow-up, and equation 2 tells us the $z = 0.6$ solution is 4.5σ [$\approx (5-2)/(0.13*5)$] removed using just the submm z_{phot}.

2.2 Robust redshifts

2.2.1 Robust redshifts from CO lines

Figure 1 shows the derivation of a spectroscopic redshift of $z_{\text{spec}} =$ 2.7, with two lines at 93.463 and 155.772 GHz, corresponding to CO3-2 and CO5-4 respectively. A high-z redshift solution ($z_{\text{spec}} =$ 6.4) exists because of the linear spacing between CO line transitions and their isotopologues, but this solution would require additional lines at 109.04 and 140.195 GHz. The lack of such emission can be used to exclude this redshift possibility.

2.2.2 Robust redshifts from CO and ancillary lines

Non-CO lines do not scale linearly with CO line emission, and thus always offer a robust derivation of the spectroscopic redshift. This is because the high fidelity of the central frequency (typically in excess of f/$\Delta f \sim 10^4$) leaves no room for multiple interpretations. In Figure 2, we show this scenario for a fiducial $z_{\text{spec}} = 2.45$ galaxy with observed C(3-2) and CI(1-0) at 100.236 and 142.645 GHz respectively.

2.2.3 Robust redshifts from single-line detections

These graphs allow us to visualize the bandwidth, and associated redshift possibilities, that our observations have covered. As shown in Figure 3, if we detect a convincingly-bright line (see Section 2.3.2) at 144.089 using our efficient ALMA tuning, we can exclude most neighbouring redshift solutions in the same vein as the exclusion of the $z_{\text{spec}} = 6.4$ solution in Fig. 1. We would have detected lines at other frequencies for all but the lowest-redshift solution ($z_{\text{spec}} = 0.6$). Using the photometric redshift as a guide, we can exclude this possiblity, leaving only $z_{\text{spec}} = 3.0$ as a solution, with the detected line being CO(5-4). We note that the $z_{\text{spec}} = 2.41$ solution of the detection of [C I] would still require a detected CO line at 101.251 GHz.
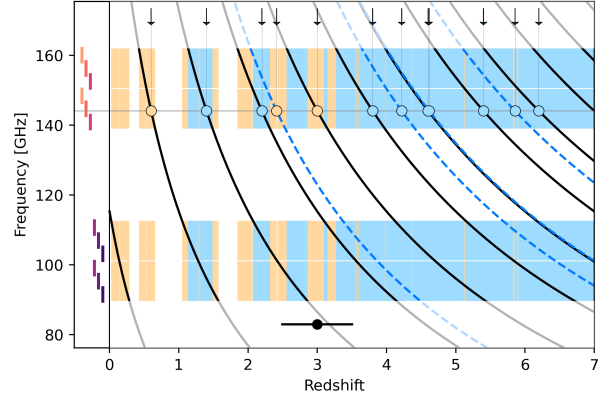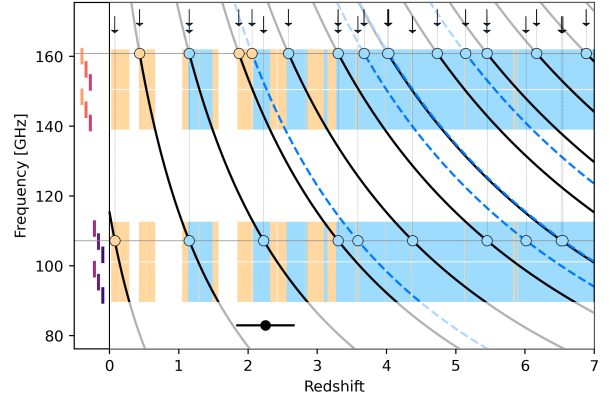

Figure 4. Same as Fig. 1, showing an inconclusive redshift from multiple detected CO lines. The detected lines at 107.229 and 160.844 GHz can correspond equally-well to $z_{\text{spec}} = 1.15$ or 3.30. Such scenarios appear when a single scalar multiplied with both CO line transitions results in other integer possibilities.

2.3 Caveats

2.3.1 Inconclusive redshifts from multiple CO lines

Unfortunately, not all solutions multi-line solutions can be excluded through the non-detection of other lines (such as in Fig. 1). We show such a scenario in Figure 4, where two redshift solutions of two lines at 107.229 and 160.844 GHz can correspond to $z_{\text{spec}} = 1.15$ or 3.30. The low-redshift scenario would detect CO(2-1) and CO(3-2), while the higher-redshift solution involves CO(4-3) and CO(6-5). Such scenarios occur when the ratio of the upper transition (J_{up}) of both CO line transitions can be multiplied to form another set of integer numbers. In this case, the common multiplier is *two*, however extensive possibilities exist. We can quantize the change in redshift between a scenario where the true solution involves either CO(a,

$a - 1$) or CO($b, b - 1$) as follows

$$\frac{\Delta z}{1 + z} = \frac{b - a}{a}. \tag{1}$$

The 1σ spread in $\Delta z/(1 + z)$ is typically on the order of 13%. In case the photometric redshift of a line agrees with a solution of CO($a, a - 1$), the photometric redshift can thus identify how many standard-deviations (N) we are offset from a solution at CO($b, b - 1$) using

$$N[\sigma] \approx \frac{b - a}{a \times 0.13}. \tag{2}$$

In case of multiple detected lines, we can identify the nearest combination of lines that can be confused for one-another. Mathematically, this multiplier can be identified using the greatest common divisor, the GCD. The nearest solutions are the multiplication of the remaining components with $GCD \pm 1$. In the case of a tentative redshift based on CO(4-3) and CO(6-5), the largest common multiplier of the CO transitions is 2, leaving additional redshift solutions using CO(2-1) and CO(4-3), as well as CO(6-5) and CO(8-7).

2.3.2 Excluding redshift regimes

We can exclude redshift regions where we would have seen lines in a deep enough survey. These are typically restricted to CO lines, since the correlation between CO lines and [C I] emission strongly depends on the particular ISM conditions (see e.g., Valentino et al. 2018). CO lines transitions, instead, are strongly correlated to one-another through transitional partition functions following so-called spectral line energy distributions (SLEDs). The Milky Way CO SLED has a sharp drop-off in velocity-integrated fluxes for higher-J transitions, however for star-bursting galaxies, these SLEDs can approach the *maximum* thermalized profile, where velocity-integrated fluxes increase with J^2 (see Carilli & Walter 2013).

In the case of Fig. 1, we know the undetected CO lines should be at least on the same order of brightness as the detected lines, as their transitions are in between the detected emission lines. For the single-line case, the $z_{\rm spec} = 2.2$ case would have, in the most unfortunate case, a CO(3-2) line with an integrated flux of $(3/4)^2 \approx 56\%$ fainter than the detected line. Similarly, for the higher-redshift solution at $z_{\rm spec} = 3.8$, the CO(5-4) would be $\sim 70\%$ ($= 5^2/6^2$) as bright as the detected line. The exclusion method thus requires relatively-high signal-to-noise ($> 8\sigma$) detections to be robust.

2.3.3 Disqualifying low-redshift interlopers

As a general rule, redshift deserts become more prevalent at lower redshifts. Observed frequencies of lines lie far apart, and relatively-narrow bandwidths cover only small Δz. For example, at $z = 0.5$, CO(1-0) is not accessible with ALMA and CO(3-2) requires band 6 (345 GHz) observations, while at $z = 4$ both CO(4-3) and CO(5-4) are covered in band 3 (3mm; ~ 100GHz). As such, low-redshift interlopers can only be excluded directly using large observed bandwidths. Another solution involves multi-wavelength observations, which become capable of detecting even heavily dust-obscured galaxies themselves and provide much more accurate photometric redshifts through optical and near-infrared spectral fits.

3 REDSHIFT SEARCHES

The graphical method facilitates the analysis once the observations are done. This Section complements this by providing a figure of

Table 1. Instruments used for redshift searches

Instrument	Observing bandwidth		
	[GHz]	/	[mm]
ALMA:	92 − 114.9 &	/	3.26 − 2.61 &
B3 & B4	125.15 − 148.05		2.40 − 2.03
Spectral scan:	84.2 − 114.9 &	/	3.56 − 2.61 &
B3 & B4	125 − 159.25		2.40 − 1.88
ALMA B3 fill	84.2 − 114.9	/	3.56 − 2.61
RSR	73 − 111	/	4.11 − 2.70
Zpectrometer	25.6 − 37.7	/	11.7 − 7.9
Z-Spec	185 − 305	/	1.62 − 0.98
DESHIMA	220 − 440	/	1.36 − 0.68
Superspec	200 − 300	/	1.50 − 1.00
OST (Band 6)	509 − 893	/	0.59 − 0.34

Notes: The top two rows together show the optimised tuning from Figure 6. The third and fourth rows together show the spectral scan set-up, assuming five stacked tunings at both 3 and 2mm.

merit for past, existing and future redshift searches. This method can then be used to optimise future redshift searches, and guide the design of instruments for future redshift surveys.

Figure 5 shows the probability of a robust redshift of various configurations and instruments that are often used for redshift searches between $z = 0$ and 8, and for two different DSFG samples (HerBS; Bakx et al. 2020a, South Pole Telescope; Reuter et al. 2020). The details of each instrument are shown in Table 1. For the calculation in Figure 5, we remove regions that are opaque under normal observing conditions (precipitable water vapour > 0.5 mm). We show the total number of sources detected robustly with multiple lines and with single lines in *blue fill and hatches*, respectively. The *orange fill and hatches* show where the redshift remained ambiguous with one or two lines, while the white region provides a measure of the redshift desert.

3.1 Interferometric redshift searches

Interferometers can serve as redshift instruments by combining multiple spectral windows while delivering high-resolution imaging of both line and continuum emission. However, the telescope array with the largest collecting area, ALMA, only offers a modest spectral coverage. While the necessary integration time to detect a line from, for example, bright Herschel source is only several minutes, an ALMA-based redshift search could thus result in large overheads due to the need to switch tunings. Generally, there are two ways around the large overheads. Firstly, ALMA offers the ability to observe sources close on the sky (typically ~ 10 degrees of separation) without the need to recalibrate. Observations can then be carried out in batches of sources, reducing the overheads per source. Secondly, ALMA recently started to offer[2] spectral scans that calibrate all spectral windows on the calibrator, cutting down significantly on slewing overheads. If the targeted source has only a couple (typically $\lesssim 4$), the spectral scan is preferred.

3.1.1 Filling the 3mm band

The initial observations of SPT sources using the full 3mm band of ALMA successfully demonstrated the interferometer's redshift search capabilities (Vieira et al. 2013; Weiß et al. 2013). These observations use five tunings with ALMA, starting at 84.2 GHz up to

---

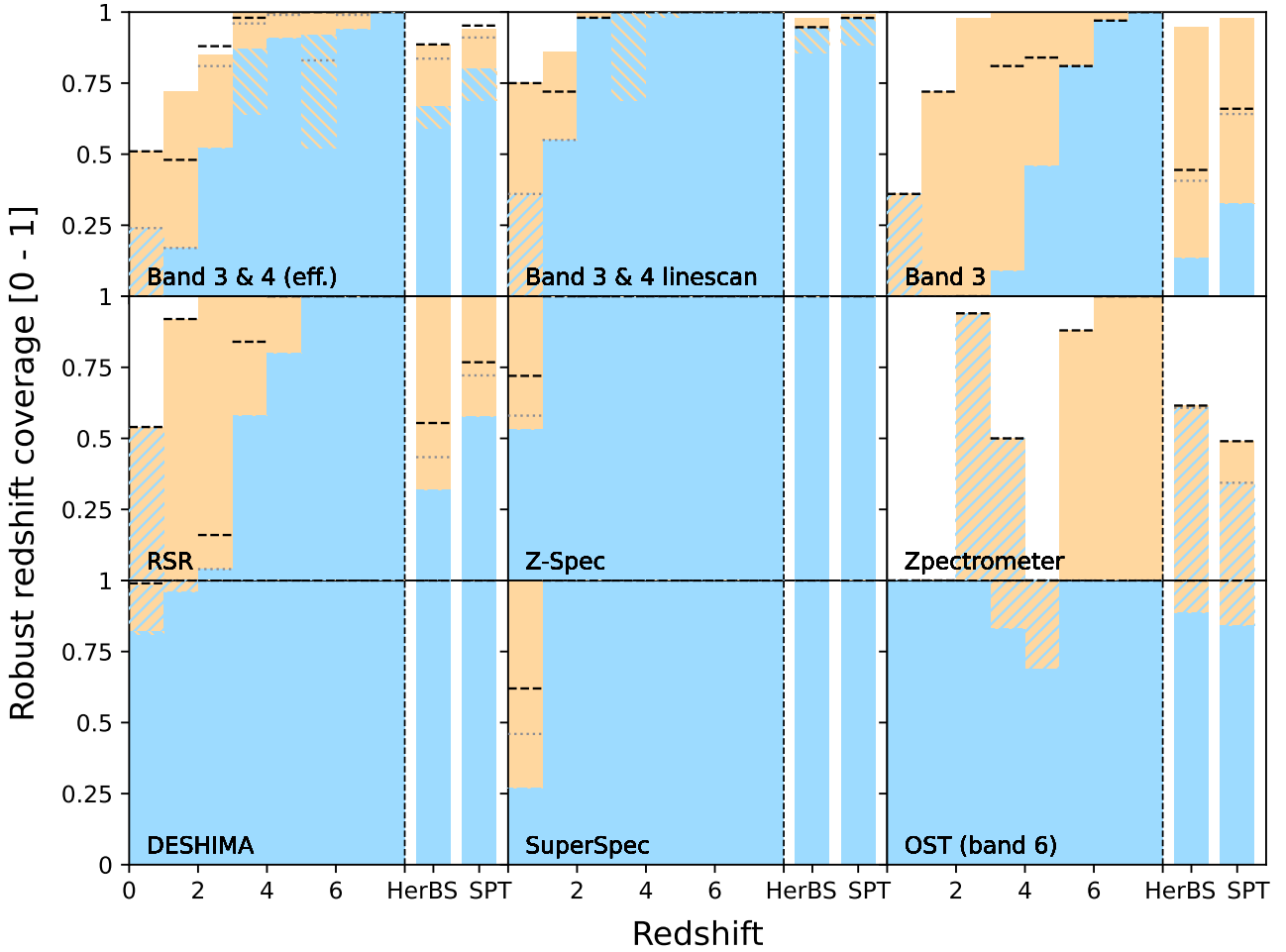[2] https://almascience.eso.org/proposing/proposers-guide

Figure 5. The robust redshift identification probability as a function of redshift between $z = 0$ and 8, and for two known redshift samples (i.e., HerBS; Bakx et al. 2018, 2020a, SPT; Reuter et al. 2020). *Orange bars* indicate the fraction one would detect a single spectral line, while *blue bars* indicate the fraction two or more spectral lines are detected. *Hatched blue fill* indicates the cases where one can identify the redshift robustly with even a single spectral line, while *hatched orange fill* indicates the situation where redshift degeneracies remain down to a 5σ uncertainty in z_{phot}. The *grey dotted lines* indicate the robust (single + multiple lines) redshifts when one expects to detect [C I], and the *black dashed lines* indicate the robust (single + multiple lines) if we only include degeneracies within 3σ from the z_{phot} value. The *top panels* indicate the redshift capabilities of various ALMA set-ups, showing an optimized Band 3 & 4 set-up (see Table 1 and Figure 6), a linescan Band 3 & 4 set-up, and the filled Band 3 tuning from Weiß et al. (2013). The *middle panels* show known redshift receivers (RSR; Erickson et al. 2007, Z-Spec; Naylor et al. 2003, Zpectrometer; Harris et al. 2007), and the *bottom panels* show the redshift capabilities of future instruments that are currently under development (DESHIMA 2.0; Taniguchi et al. 2021; Rybak et al. 2021, SuperSpec; Redford et al. 2021, Origin Space Telescope (band 6); Bradford et al. 2021).

114.9 GHz with overlapping coverage between $96.2 - 102.8$ GHz. Figure 5 shows that, while these observations are able to guarantee a single-line detection above $z > 2$, this tuning provides only moderate ability to derive robust, unambiguous redshifts on the CO emission alone. [C I] emission, as well as improved photometric redshifts can vastly improve the ability of this configuration to estimate the redshift, particularly for samples biased towards high redshifts. Meanwhile, these observations target the CO emission up to the CO(6-5) rotational transition (with one exception up to CO(7-6); Marrone et al. 2018). It is good to note that these emission lines correlate with the far-infrared luminosity – which is often a direct selection function for high-redshift DSFGs – and these observations are thus less likely to bias observations. Instead, observations aiming at higher-J

transitions might be particularly-sensitive to the warmer and denser molecular gas typically found in AGN (e.g., Xu et al. 2014).

3.1.2 Combined 3 and 2mm tunings

We test the ability to include 2mm tunings to improve the robust redshift coverage of ALMA. This configuration uses two near-contiguous frequency coverages at both 3 and 2mm, which removes the overlapping region of the 3mm scan. Figure 6 shows the redshift coverage for each possible combination of 3 and 2mm regions. The efficiency between the possible configurations varies between 0.4 to 0.6 for different combinations, with the optimum lying at the higher frequencies in band 3 (3mm; although one should be careful about
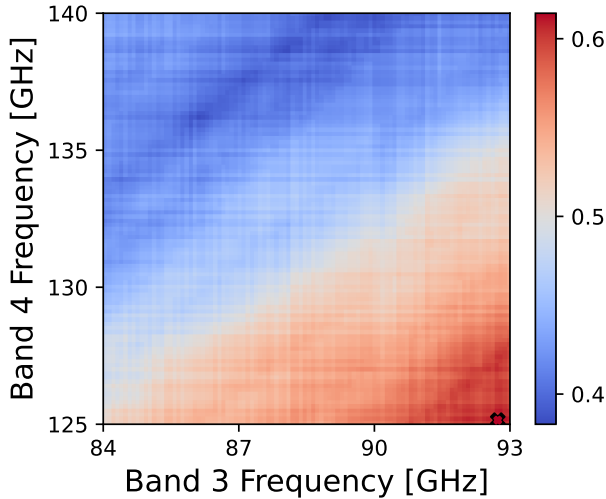
Figure 6. The distribution in robust redshift probability for different band 3 and 4 (3 and 2mm, resp.) configurations for HerBS targets (Bakx et al. 2018). Here, we assume a 'stacked' configuration of three spectral windows in each of the respective bands, starting at the documented value. The optimum observing frequencies for such a combined band 3 and 4 observation with ALMA lie at the high-frequency end of the 3mm window and at the lower-frequency end of the 2mm window, as marked with the *red cross*.

the absorption line beyond 115 GHz) and at lower frequencies in band 4 (2mm).

3.1.3 ALMA spectral scans

Recent development at ALMA allowed for efficient observations of multiple (up to five) spectral windows for a single source. By calibrating all spectral windows in one go, this observing strategy cuts down significantly on the overheads. We note here that a scan of just band 3 results in similar redshift coverage issues as seen in Figure 5, as well as the large overlapping coverage seen in e.g., Weiß et al. (2013). The coverage issue, however, can be mitigated by including a spectral scan in band 4, which vastly improves the redshift coverage across a wide range of redshifts.

3.1.4 NOEMA redshift searches

Unlike ALMA, NOrthern Extended Millimeter Array (NOEMA) and the IRAM 30m (e.g., Bakx et al. 2020b) offer the ability to adjust the bandwidth dynamically, based on observed spectral lines in other tunings (e.g., Neri et al. 2020). The wider bandwidths (up to ∼ 16 GHz in one tuning, with possible expansion in the future) allow for a wide 3mm scan in just two tunings. Typically (see the 3mm scan in Figure 5) one requires additional observations in the 2mm band. Follow-up observations in the 2mm band do not lend themselves for easy generalization, which is why we were not able to generate a similar plot for a NOEMA 3- and 2mm redshift search. Nevertheless, the graphical method of this paper (i.e., Fig. 1) can offer significant aid in determining additional observations at both 2mm and other bands, while also highlighting redshift degeneracies.

3.2 Dedicated redshift receivers

The advent of spectrometers with instantaneous wide-band enabled the first large-scale redshift surveys. While the first submm redshift searches involved heterodyne instruments with requiring multiple tunings (e.g., Weiß et al. 2009), the notable instruments that performed these dedicated redshift searches are the Redshift Search Receiver (RSR; Erickson et al. 2007), Z-Spec (Naylor et al. 2003), and Zpectrometer (Harris et al. 2007).

3.2.1 Redshift Search Receiver

The Large Millimeter Telescope (LMT)-based observations combine the instantaneous coverage of the 3mm window with the powerful 32 to 50 m diameter of the telescope to reveal the spectral lines of galaxies out to high redshifts (e.g., Zavala et al. 2015, 2018). At lower redshifts particularly, these observations require ancillary data – such as with IRAM or VLT – to confirm the redshifts robustly. The addition of a 2mm spectroscopic ability at the LMT would significantly increase the telescope's ability to determine redshifts robustly.

3.2.2 Z-Spec

The wide bandwidth capability of Z-Spec at 1.0 to 1.6 mm enabled the near-guaranteed ability to detect more than one spectral line. As seen in Lupu et al. (2012), the higher-frequency transitions (often of CO lines) are not guaranteed. In this case, clever stacking of the line emission as a function of redshift enabled robust redshifts even though individual lines might be detected only at a few sigma. It is good to note that, unlike the RSR and Zpectrometer, the diameter of the Caltech Submillimeter Observatory (CSO) where the telescope operated was modest at 10 m, since high surface accuracy needed to be guaranteed given the higher-frequency observations.

3.2.3 Zpectrometer

This receiver operated on the 100 m Green Bank Telescope, and principally targeted CO(1-0) and CO(2-1). This large collecting area is crucial, since the expected emission from these low-excitation rotational transitions is weak (Harris et al. 2010). Observationally, the GBT/Zpectrometer set-up had another advantage to increase its efficiency. While performing on-off chopping to remove background and atmospheric noise, the telescope chopped between two galaxy positions. The emission line from the second ('off') source would then be seen as a negative signal (Harris et al. 2012; Frayer et al. 2011). This method allows for the easy identification of redshifts between 2 and 3.5, as well as above 5. Interestingly, the typical uncertainty on photometric redshifts increases with redshift (going as ∼ $0.13(1 + z_{phot})$, the lower redshifts are basically robust (hatched blue), while the higher redshifts might be mis-interpreted CO(2-1) line emission that is instead CO(1-0).

3.3 Future instrumentation

New instrumentation is underway to explore the high-redshift Universe using broad-band spectrometers, in particular using Microwave Kinetic Inductance Detectors (MKIDs; Day et al. 2003; Endo et al. 2019) technology, and on-board of the Origin Space Telescope (OST; Battersby et al. 2018).

3.3.1 *DESHIMA*

The DEep Spectroscopic HIgh-redshift MApper instrument combines an integrated super-conducting spectrometer with a read-out based on MKIDs to enable ultra-wideband (> 100 GHz) spectroscopy at medium resolution ($f/\Delta f \approx 500$). We carefully exclude frequency regions with strong atmospheric absorption from our analysis in Figure 5. As shown in detail in Rybak et al. (2021), the wide bandwidth at 1.4 to 0.7 mm means that DESHIMA will be sensitive to mid- to higher-J transitions for sources at $z < 3.3$. These emission lines vary strongly from source to source, however can be brought out through similar stacking as seen in Z-Spec (e.g., Lupu et al. 2012). Beyond $z > 3.3$, the [CII] emission line will dominate the emission and will be readily detected. Notably, the robust redshift coverage of DESHIMA at even the lowest redshifts is high.

3.3.2 *SuperSpec*

The SuperSpec instrument aims to use a lithographically-patterned filterbank (similar to DESHIMA) to probe the high-redshift Universe, primarily through atomic lines of high-redshift targets between $z = 4 - 8$ (Redford et al. 2021). Its intended telescope will be the LMT, whose large collecting area allows for deep integration on even faint targets. Similar to DESHIMA, this instrument also has the ability to rapidly assess the redshifts of lower-z targets through mid-J emission lines.

3.3.3 *Origin Space Telescope*

We chose to only model the longest-wavelength band of the medium-resolution spectroscopic instrument on the OST (band 6; $0.34 - 0.59$ mm) since it is more sensitive to lower-frequency lines such as CO. We note that additional bands (which are expected to be able to observe simultaneously) improve the redshift capabilities further by picking up ancillary atomic lines which further aid in the determination of robust redshifts. Beyond $z > 1.1$, OST will be able to target [CII] emission, leaving only a little gap ($2.73 < z < 2.81$) where at band 6 is unable to pick up either [OIII]88μmor [CII]158μm, although [NII]122μmcould also be observed.

4 CONCLUSIONS

We report an efficient method for identifying redshifts, and provide a comprehensive overview of all caveats in deriving redshifts using submm spectral lines in the high-z. This method readily removes the need for cross-comparison of tables by providing a graphical overview of the explored redshift regions. Meanwhile, it provides insight into the explored regions in redshift-space, allowing for the efficient removal of untenable redshift options, while also highlighting potential redshift degeneracies. This method is expanded to calculate the capabilities of various instruments in deriving spectroscopic redshifts. We suggest optimised tunings for ALMA, stressing the need for both 3 and 2mm observations to identify robust redshifts.

DATA AVAILABILITY

All code used to derive the graphs in this paper are available at https://github.com/tjlcbakx/redshift-search-graphs in order to assist in the robust classification of redshifts in ongoing, future and past programs.

REFERENCES

Bakx T. J. L. C., et al., 2018, MNRAS, 473, 1751
Bakx T. J. L. C., et al., 2020a, MNRAS, 494, 10
Bakx T. J. L. C., et al., 2020b, MNRAS, 496, 2372
Battersby C., et al., 2018, Nature Astronomy, 2, 596
Blain A. W., Smail I., Ivison R. J., Kneib J. P., Frayer D. T., 2002, Phys. Rep., 369, 111
Bradford C. M., et al., 2021, Journal of Astronomical Telescopes, Instruments, and Systems, 7, 011017
Carilli C. L., Walter F., 2013, ARA&A, 51, 105
Casey C. M., 2020, ApJ, 900, 68
Casey C. M., et al., 2012, ApJ, 761, 140
Casey C. M., Narayanan D., Cooray A., 2014, Phys. Rep., 541, 45
Casey C. M., et al., 2018, ApJ, 862, 77
Chapman S. C., et al., 2015, MNRAS, 453, 951
Day P. K., LeDuc H. G., Mazin B. A., Vayonakis A., Zmuidzinas J., 2003, Nature, 425, 817
Endo A., et al., 2019, Nature Astronomy, 3, 989
Erickson N., Narayanan G., Goeller R., Grosslein R., 2007, in Baker A. J., Glenn J., Harris A. I., Mangum J. G., Yun M. S., eds, Astronomical Society of the Pacific Conference Series Vol. 375, From Z-Machines to ALMA: (Sub)Millimeter Spectroscopy of Galaxies. p. 71
Frayer D. T., et al., 2011, ApJ, 726, L22
Harris A. I., et al., 2007, in Baker A. J., Glenn J., Harris A. I., Mangum J. G., Yun M. S., eds, Astronomical Society of the Pacific Conference Series Vol. 375, From Z-Machines to ALMA: (Sub)Millimeter Spectroscopy of Galaxies. p. 82
Harris A. I., Baker A. J., Zonak S. G., Sharon C. E., Genzel R., Rauch K., Watts G., Creager R., 2010, ApJ, 723, 1139
Harris A. I., et al., 2012, ApJ, 752, 152
Ivison R. J., et al., 2016, ApJ, 832, 78
Lupu R. E., et al., 2012, ApJ, 757, 135
Marrone D. P., et al., 2018, Nature, 553, 51
Naylor B. J., et al., 2003, in Phillips T. G., Zmuidzinas J., eds, Society of Photo-Optical Instrumentation Engineers (SPIE) Conference Series Vol. 4855, Millimeter and Submillimeter Detectors for Astronomy. pp 239–248, doi:10.1117/12.459419
Neri R., et al., 2020, A&A, 635, A7
Pearson E. A., et al., 2013, MNRAS, 435, 2753
Redford J., et al., 2021, in American Astronomical Society Meeting Abstracts. p. 317.01
Reuter C., et al., 2020, ApJ, 902, 78
Rowan-Robinson M., et al., 2016, MNRAS, 461, 1100
Rybak M., et al., 2021, arXiv e-prints, p. arXiv:2111.05261
Taniguchi A., et al., 2021, arXiv e-prints, p. arXiv:2110.14656
Valentino F., et al., 2018, ApJ, 869, 27
Vieira J. D., et al., 2013, Nature, 495, 344
Weiß A., et al., 2009, ApJ, 707, 1201

Weiß A., et al., 2013, ApJ, 767, 88

Xu C., et al., 2014, The Astrophysical Journal, 787

Yanai I., Lercher M., 2020, Genome Biology, 21, 231

Zavala J. A., et al., 2015, MNRAS, 452, 1140

Zavala J. A., et al., 2018, Nature Astronomy, 2, 56

This paper has been typeset from a TEX/LATEX file prepared by the author.